Geophysical Prospecting EAGE EUROPEAN ASSOCIATION OF GEOSCIENTISTS & ENGINEERS

Geophysical Prospecting, 2013, **61**, 341–362 doi: 10.1111/1365-2478.12028

Specific surface area and pore-size distribution in clays and shales

Utpalendu Kuila* and Manika Prasad

Colorado School of Mines, 1500 Illinois St. Golden, CO 80401

Received February 2012, revision accepted December 2012

ABSTRACT

One of the biggest challenges in estimating the elastic, transport and storage properties of shales has been a lack of understanding of their complete pore structure. The shale matrix is predominantly composed of micropores (pores less than 2 nm diameter) and mesopores (pores with 2–50 nm diameter). These small pores in the shale matrix are mainly associated with clay minerals and organic matter and comprehending the controls of these clays and organic matter on the pore-size distribution is critical to understand the shale pore network. Historically, mercury intrusion techniques are used for pore-size analysis of conventional reservoirs. However, for unconventional shale reservoirs, very high pressures (> 414 MPa (60 000 psi)) would be required for mercury to access the full pore structure, which has potential pitfalls. Current instrumental limitations do not allow reliable measurement of significant portions of the total pore volume in shales. Nitrogen gas-adsorption techniques can be used to characterize materials dominated by micro- and mesopores (2–50 nm). A limitation of this technique is that it fails to measure large pores (diameter >200 nm). We use a nitrogen gas-adsorption technique to study the micro- and mesopores in shales and clays and compare the results from conventional mercury porosimetry techniques.

Our results on pure clay minerals and natural shales show that (i) they have a multiscale pore structure at different dimensions (ii) fine mesopores, with a characteristic 3 nm pore size obtained with N_2 gas-adsorption are associated with an illite-smectite group of clays but not with kaolinite; (iii) compaction results in a decrease of pore volume and a reduction of pore size in the 'inter-aggregate' macropores of the illite-smectite clays while the fine 'intra-tachoid' mesopores are shielded from compaction; (iv) for natural shales, mineralogy controls the pore-size distributions for shales and the presence of micropores and fine mesopores in natural shales can be correlated with the dominance of the illite-smectite type of clays in the rock. Our assessment of incompressible 3 nm sized pores associated with illite-smectite clays provides an important building block for their mineral modulus.

Key words: Clays, Shales, Pore-size distribution, Specific surface area.

INTRODUCTION

The most common sedimentary rocks on the Earth's crust are shales, constituting over 75% of the clastic fill in sedimentary basins. In conventional petroleum plays, organic-rich shales are the source rocks for petroleum generation. They are also the seals in a clastic trap. In reservoir engineering, shales are the flow barriers and in seismic data they can be seismic reflectors. In a petrophysical analysis of conventional reservoirs, the log responses are calibrated with the regional water-saturated shale layers. Over the past decade, interest in shale reservoirs has increased due to the commercial success of gas-shale plays. In contrast to conventional

*E-mail: ukuila@mines.edu

plays, these plays typically have very fine-grained rock texture (dominant grain size $\leq 62.5\ \mu$m), low porosity ($\leq 10\%$) and very low permeabilities (in the nanodarcy range). These are source rocks with high organic content ($\geq 2\%$ weight fraction, Total Organic Carbon, TOC) that also function as reservoir rocks. Gas reserves in these plays are huge, estimated to be ~1000 trillion cubic feet (TCF) in North America and ~200 TCF in Europe (Jaffe 2010). A recent U.S. Energy Information Administration (EIA) (2012) report states that in the U.S. shale gas production will increase from 5.0 TCF in 2010 to 13.6 TCF in 2035, making it about 49% of the total U.S. natural gas production. Despite the commercial importance of shale formations, their physical properties, especially porosity and pore-size distributions, are still poorly understood.

Porosity and pore-size distribution (PSD) are the most important aspects of a porous medium and affects most behaviour of porous media, e.g., elastic and mechanical behaviour, movement and flow of fluids etc. Shales have a more complex pore structure than conventional reservoir rocks like sandstones and limestones. The most distinctive characteristic of shales is their multiscale fabric that can be linked to the microstructure of clay minerals. Studies on pure clay minerals, especially smectite, have revealed multiple scales of structure: several individual elementary units comprising aluminosilicate tetrahedral-octahedral-tetrahedral (TOT) layers with interlayer cation (9–10 Å) form mesoscopic 'tachoids' or 'quasicrystals' (2–50 nm) (Aylmore and Quirk 1971; Cases *et al.* 1992; Neaman, Pelletier and Villieras 2003; Jullien *et al.* 2005). These tachoids are bundled together to form macroscopic clay platelets or 'aggregates' (~1 micron) (Aylmore and Quirk 1971; Cases *et al.* 1992; Neaman *et al.* 2003; Jullien *et al.* 2005). In shales, these clay aggregates form a locally aligned matrix with varying orientations, depending upon the depositional and stress history of the rock and silt content (Hornby *et al.* 1994; Arne Johansen, Ruud and Jakobsen 2004; Sayers 2005). These multiple scales are associated with porosity with different dimensions and scales. One of the biggest challenges in estimating the elastic and transport properties of shales has been a lack of understanding of their complete pore-size distributions. The mismatch between the measured and predicted elastic stiffness coefficients of shales by over a factor of two, lies in inadequate microstructural representations (Militzer *et al.* 2011). Clay-water composites are used as the building unit for rock-physics modelling of shales (Hornby *et al.* 1994; Arne Johansen *et al.* 2004). However, most of the application of these models to natural shales concentrate on the orientation distribution function of macroscopic clay 'aggregates' but fail to incorporate the associated multiscale pore volumes, particularly mesoscopic porosity and their evolution under increasing stress. 'Hard' data on the pore-size distribution of clays in pure form and in shales will be a valuable input for the rock-physics models of shales.

Pore-size distribution in any porous media controls the transport behaviour of fluids through them. In gas-shale plays, gas flow occurs mainly through an interconnected fracture network system. This fracture network system is postulated to be recharged by gas flowing through the shale matrix dominated by micropores (pores smaller than 2 nm as per International Union of Pure and Applied Chemistry (IUPAC) classification) to mesopores (pore size from 2–50 nm as per IUPAC classification). The Darcy model of permeability and flow that is applied in conventional plays cannot be directly applied to shale reservoirs due to the presence of these small pores. Gas production from these resources is much greater than anticipated and cannot be described by conventional wisdom. Gas flow in the nanoporous shale matrix is expected to be a combination of Knudsen diffusion and slip flow in nanometre-sized pores and Darcy-like flow in micrometre or larger size pores. Modelling this flow requires knowledge about the pore diameters and their distribution.

Most porosity and pore-size distribution measurement techniques involve removing or displacing naturally occurring formation fluids or gas with a measurable quantity of an introduced gas or liquid into the pore system of a sample. Such measurements in shales become complicated because of the very fine-grained texture, small pore sizes, extremely low permeability and the strong interaction of water with the structure of clay minerals, which are often the major components in these rock types. Historically, mercury intrusion porosimetry (MIP) is used for pore-size analysis of macroporous conventional reservoirs. The current instrumental limitation for MIP (pressures up to 414 MPa (60 000 psi)) cannot theoretically measure pores smaller than 3.6 nm, while the practical limit is probably higher. Significant populations of pores in shales are too small to be measured by MIP, which explains the underestimation of the total connected pore volume as compared to helium pycnometry measurements. Bustin *et al.* (2008) pointed out the potential pitfalls of using very high mercury injection pressures to obtain the pore-size distribution in shales. The compressibility of the rock structure, the possibility of breaking the particles and opening closed pores will affect the data collected at such high pressures. Subcritical gas-adsorption techniques are widely used in the chemical, ceramic and pharmaceutical industries to characterize the pore structure and the specific surface areas of powders and fine microporous materials such as activated carbon, carbon

nanotubes, zeolites and catalysts. Different gases, such as nitrogen, argon and carbon dioxide, are used to investigate very fine pores in the range of 0.3–200 nm. Nitrogen is the most widely used gas for such experiments and it works well for materials dominated by mesopores (2–50 nm). A limitation of this techniques is that it fails to measure large pores (diameter >200 nm). A combination of mercury intrusion and nitrogen gas-adsorption gives us information for the entire pore structure. However, a direct comparison of the pore volumes from these two different techniques is not advised because nitrogen gas and mercury record pore structures differently. The intrusion of mercury in the pore structure is controlled by pore throats (the smallest dimension in an irregular pore) while the adsorption phenomenon during the subcritical N_2 gas-adsorption technique is controlled by the pore body. Combining information from these two techniques provides complementary information about the pore structure of any porous media.

Comprehending the controls of clays and organic matter on the pore-size distribution is critical in order to understand the shale pore network. In this paper, we will present pore-size distribution results obtained from nitrogen gas-adsorption on clays and natural shales. Mercury intrusion techniques were used to compare the results obtained from N_2 gas-adsorption. We will discuss the implications and controls that end-members like clays exert on the pore-size distributions of natural shales and what effects these pore-size distributions can have on their elastic properties. Our study provides critical data characterizing the pore structure in shales for input to rock-physics and flow modelling, as well as a fundamental understanding of compositional controls on the pore structure in shales.

PPREVIOUS STUDIES

In the literature, a wide variety of terminology is used to classify small pores (for example, nanopores, mesopores, micropores, etc.). Moreover, 'pore size' does not have a very precise definition due to the highly irregular, variable interconnected network nature of pores. Quantitative descriptions of pore structure are usually based on model assumptions. Since our inversion of pore volumes assumes cylindrical pore geometry, 'pore size' in this paper refers to the diameter of an equivalent cylindrical pore. The International Union of Pure and Applied Chemistry (IUPAC) recommend the following classification of pores according to their size:

1. Micropores: pores with pore size below 2 nm
2. Mesopores: pores with pore size between 2–50 nm
3. Macropores: pores with pore size greater than 50 nm

The advantage of this classification is that it is based on the physics of nitrogen adsorption in various pore sizes of a porous material at −197.3°C (77.3°K) and 1 atmosphere pressure. Different mechanisms, such as multilayer adsorption, capillary condensation and micropore filling dominate in macropores, mesopores and micropores, respectively. The disadvantage is that the classification is not intuitive; nano-sized pores are termed as micropores and mesopores. Additionally, pores larger than 50 nm are not subdivided further. They are jointly classified as macropores. However, since the IUPAC classification (Sing 1985) is a non-arbitrary classification, we will use the IUPAC pore-size classification for this paper. The IUPAC classification is more appropriate for shales since we expect shales to have a considerable volume of their pore space in nanometre-sized pores. For future work, we recommend defining a pore size classification that is more appropriate for shale-reservoir rocks.

The pore structure of pure clays are studied in detail using several measurement techniques including advanced imaging techniques, such as transmission electron microscopy (e.g., Kim *et al.* 1995; Jullien *et al.* 2005), scanning electron microscopy; gas-adsorption techniques (Aylmore and Quirk 1971; Cases *et al.* 1992; Rutherford, Chiou and Eberl 1997; Neaman *et al.* 2003) and MIP techniques (Diamond 1970; Ahmed, Lovell and Diamond 1974). The pore volume, specific surface area and pore sizes of clays, particularly smectites, depend mainly on the origin of the sample, layer charge or cation exchange capacity, nature of the exchanged cation and the drying and/or dehydration conditions during sample preparation. In their study of pure-homoionic smectite clays with N_2 and neo-hexane adsorption techniques, Rutherford *et al.* (1997) reported that depending on the cation, micropores make up 14–66% of the total pore volume. Pores of different sizes associated with the multiscale stacked structure of clays have been reported. Micropores in smectites are associated with slit-shaped or wedged pores on the broken edges or overlapping regions of the turbostatically stacked elementary unit within 'tachoids' or 'quasicrystals' (Aylmore and Quirk 1971; Cases *et al.* 1992; Neaman *et al.* 2003). The tachoids stack to form aggregates, which results in 'intertactoid' small and medium mesopores (Neaman *et al.* 2003; Jullien *et al.* 2005). Stacking of aggregates with preferred alignment form inter-aggregate pores, which are usually in the micron size range (macropores >50 nm). Neaman *et al.* 2003 reported that compaction of pure smectites resulting in a reduction of pore volume corresponds to inter-tactoid and inter-aggregate

pores. Diamond (1970) reported the presence of micron-sized pores in clays using the MIP technique.

The presence of micropores and mesopores in a shale matrix has been documented in several studies. Connell-Madore and Katsube (2006) reported pore-size distribution for shales from the Beaufort-McKenzie Basin and Scotian Shelf using the MIP technique. They reported unimodal pore (throat)-size distribution with the modal size decreasing with compaction. Their reported modal size was between 25 nm to 10 μm at a shallow burial depth and between 2.5–25 nm at deep burial. Ewy and Morton (2009) also reported bimodal to unimodal pore (throat)-size distributions from MIP measurements on artificial shale pellets compacted in the laboratory. Bustin *et al.* (2008) recommended using a combination of gas-adsorption and MIP for shales to overcome the problems associated with the inability of gas-adsorption techniques and high-pressure mercury intrusion to capture large and small pores. They reported bimodal size distributions with modes at 10 nm and others around 10 000 nm for Barnett and Antrim formation shale using a combination of MIP, N_2 and CO_2 adsorption techniques. However, the authors did not distinguish between the pore-throat and pore-body size distributions obtained by the different techniques but acknowledged the disagreement in pore volume in the overlapping region due to different theoretical assumptions used in the inversion. Ross and Bustin (2009) studied the pore structure of Devonian-Mississippian and Jurassic shales from the Western Canadian Sedimentary Basin using the combined technique. They reported a good correlation between micropore volumes and the TOC content of organic rich shales, a positive correlation between clay content and total MIP-porosity and a systematic change in pore structure with increasing clays. More recently, advanced imaging techniques have allowed imaging a small pore structure of nanometre scale in clays and kerogen. Javadpour (2009) used the Atomic Force Microscopy technique to show pores and grooves with dimensions of about a few nanometres associated with clays. Loucks *et al.* (2009) showed back-scattered SEM images of nanometre-scale pores associated with clays and kerogen in Barnett Shale and revealed pores as small as 4 nm. These studies suggest that the small pores in shales are associated with clays and kerogen. A systematic study to understand the compositional controls on the pore structure of shales by characterizing the pore structure of shales and its compositional end members, like clays and kerogen, is still lacking. This study focuses on understanding the pore structure in clay minerals as powders and as compacted samples and on comparing these end-member results with pore-size distributions in natural shales.

THEORETICAL CONSIDERATION

Low-pressure gas-adsorption experiments are used to obtain information about specific surface areas, micropore volumes and pore-size distributions for pores with a diameter less than 200 nm. In this section, we will discuss the different techniques used to estimate these parameters from gas-adsorption isotherms.

Nitrogen gas-adsorption experiment and isotherms

In a gas-adsorption experiment, a degassed sample is exposed to nitrogen gas at constant cryogenic liquid nitrogen (LN_2) temperature (-197.3°C) at a series of precisely controlled pressures. The volume of adsorbed gas on the solid surface is measured at discrete pressures over the relative equilibrium adsorption pressure (P/Po) range of 0.075–1.0 at a constant temperature, where P is the absolute equilibrium pressure and Po is the condensation pressure of nitrogen at laboratory conditions. The experiment is carried out by systematically increasing the pressure up to the condensation pressure (adsorption branch) followed by reduction of pressure from Po (desorption branch). The gas-adsorption isotherm is reported as the volume of gas adsorbed as a function of P/Po. The shape of the isotherm and the hysteresis pattern provide useful information regarding the mechanism of the physisorption process and hence can be used to qualitatively predict the types of pores present in the adsorbent. The IUPAC classifies the adsorption isotherms into six types: Type I to Type VI and the hysteresis patterns into four types: Type H1 to Type H4. For this work, three types of isotherms are relevant. A purely microporous adsorbent will exhibit a concave shape isotherm with very high adsorption at low-relative pressure ($P/Po < 0.01$) before it reaches a plateau (Type I isotherm, Fig. 1a). A non-porous or a macroporous material will exhibit a completely reversible isotherm (Type II isotherm, Fig. 1b) i.e., adsorption and desorption have the same path. The isotherm initially has a concave shape at lower relative pressures ($P/Po < 0.2$), followed by a linear region and finally a convex shape to the P/Po axis at higher relative pressure ($P/Po > 0.4$). A purely mesoporous material will have a hysteresis loop, which is associated with capillary condensation and evaporation taking place in mesopores and at higher P/Po it exhibits as a plateau or limiting adsorption indicating completion of mesopores filling (Type IV isotherm, Fig. 1c). A detailed description of the isotherm classification suggested by IUPAC is presented in Sing (1985) and Rouquerol, Rouquerol and Sing (1998).

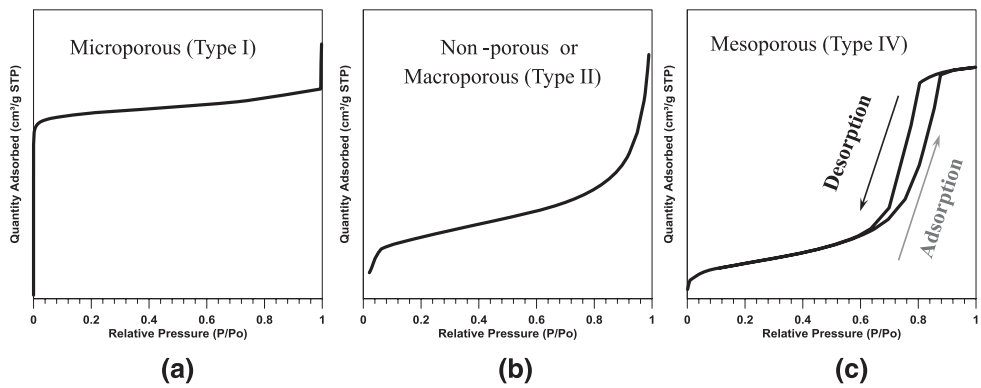

Figure 1 Typical isotherm shape exhibited by (a) purely microporous material (Type I, isotherm profile) (b) non-porous and macroporous material (Type II, isotherm profile) and (c) purely mesoporous materials (Type IV, isotherm profile).

The adsorption of gas in a porous material occurs through a number of different mechanisms, which are dominant at different relative pressures. At extremely low-relative pressures (P/Po < 0.01), all the micropores (if any) will exhibit micropore filling due to enhanced adsorbent-adsorbate interaction. The adsorbed amount will depend upon the micropore volume present in the sample. In mesopores and macropores, multilayer adsorption onto the pore walls happens initially in the approximate relative pressure range of 0.05–0.30. Generally a sharp knee-bend is observed in the isotherm indicating the completion of single molecular layer (monolayer) coverage of adsorbate molecules on the available pore surface and the beginning of the formation of the multi-molecular layer. This multilayer adsorption enables the measurement of a specific surface area of the porous material, because the amount of gas adsorbed will be proportional to the surface area available for adsorption. At higher relative pressure (above 0.4 P/Po), the gas condenses in the pores to a bulk liquid phase by a mechanism known as capillary condensation. The gas in the pores condenses at pressures, which are dependent on the pore diameter, below the saturated vapour pressure of the gas (Po). Thus, gas in pores with different diameters will condense at different pressures and this can give us information about the distribution of pore sizes present in the sample. Another important feature observed on many hysteretic patterns is the forced closure of the desorption branch where the isotherm 'closes' at P/Po around 0.35–0.45 for N2 isotherms. This phenomenon is attributed to a process called the 'Tensile Strength Effect'. Sudden disappearance of the hysteresis around this particular relative pressure range is attributed to the collapse of the hemispherical meniscus during capillary evaporation in pores with diameters less than approximately 4 nm (Groen, Peffer and Pérez-Ramírez 2003). The surface tension forces are larger than the tensile strength of the liquid and hence the meniscus collapses. Presence of this 'forced closure' in the isotherm shape indicates the presence of small pores with diameters less than 4 nm in the samples.

Specific surface area determination

For a specific surface area (surface area per unit gram) measurement, the adsorption isotherm was inverted using the BET (Brunauer, Emmett and Teller) theory. This theory suggests using a transform plot to determine the statistical 'monolayer capacity', which is the amount (moles) of nitrogen required to cover the total surface area (i.e., the external surface area and the surface area caused by meso- and macropores) with a complete monolayer of nitrogen molecules. The 'monolayer capacity' is then converted into a specific surface area by multiplying it with the average cross-sectional area occupied by each N_2 molecule at $-197.3°C$ (0.162 nm^2, as suggested by ISO 9277:2010) and the Avogadro constant (number of molecules in one mole, 6.023E+23). Brunauer, Emmett and Teller (1938) showed that this transform plot has a linear trend with a positive intercept over the region of multilayer adsorption, which happens in the approximate P/Po range of 0.05–0.30 for various materials. However this range is highly debated (Gregg and Sing 1983; Rouquerol *et al.* 1998); the linear range being more restricted depending upon the nature of the material. While the classical BET transform range (P/Po = 0.05–0.30) is appropriate for nonporous, mesoporous and macroporous materials, it fails for material containing micropores (Rouquerol, Llewellyn and Rouquerol 2007). This is because theoretically the BET theory is not applicable for micropores (<2 nm pore width) where nitrogen is adsorbed by the micropore filling phenomenon instead of multilayer adsorption. A modified BET approach was suggested by Rouquerol *et al.* (2007) to evaluate surface areas for materials

containing micropores. However, the authors pointed out that these values should not treated as an 'equivalent surface area' or the absolute 'true' surface area, because the theoretical basis of the BET theory and 'monolayer capacity' does not explain nitrogen adsorbent behaviour in micropores. The advantages of this method are that it reduces any subjectivity in the assessment of the fitting range of the BET plot and gives an objective way to determine the fitting range of the BET transform plot rather than using the same relative pressure range for all materials. The modified BET technique, as suggested by Rouquerol *et al.* (2007), has been adopted in ISO 9277:2010 and was followed in this study.

Assessment of pore volume and distribution

The total pore volume for the subcritical N_2 gas-adsorption technique was obtained from the general principle of Gurevich rule (Gregg and Sing 1983; Rouquerol *et al.* 1999). The specific pore volume is obtained by the liquid molar volume adsorbed at a predetermined P/Po. The liquid molar volume adsorbed at the relative pressure (P/Po) of 0.99 is calculated by converting the adsorbed gas volume to the liquid molar volume using a N2 density of 0.808 g/mL. A relative pressure of 0.99 corresponds to a pore size (diameter) of 193.5 nm and hence the total pore volume indicated is the pore volume of pores smaller than 193.5 nm diameter. The t-plot is a technique used widely to estimate the micropore volume and 'the open surface area', the surface area from mesopores, macropores and the external surface area (the total surface area excluding the surface area of micropores). In t-plots, the adsorbed N_2 volume (V_a) is plotted against the statistical thickness (t) of the adsorbed layer of N_2. Several thickness equations have been proposed in the literature as a representative 'universal thickness curve' of which the most generally applicable and most frequently employed are those of Harkins-Jura, Halsey and Broekhoff-de Boer (Webb and Orr 1997). In this study, the universal t-curve of N_2 of Harkins-Jura (Webb and Orr 1997) is used.

The pore-size distribution is obtained by the application of the BJH (Barret, Joyner and Halenda) technique, assuming cylindrical pore geometry. Capillary condensation happens after multilayer adsorption from the vapour phase during which the mesopores are filled with bulk liquid separated from the gas phase by a meniscus. The Kelvin equation, which describes the effect of the surface curvature of the liquid-vapour meniscus on the vapour pressure, relates the pore diameter with the relative pressure (P/Po). However, capillary condensation takes place after multilayer adsorption and the pore walls are already coated with multilayers of adsorbed gas molecules. The thickness of the adsorbed layer, t, will depend upon P/Po and has to be accounted for while inverting for the volume adsorbed data to pore volumes. The BJH technique suggests an algorithm to invert the measured isotherm data using Kelvin's equation by incorporating the effect of the thinning of the adsorbed layer through thickness curves. In this paper, the Harkins-Jura thickness curve is used to be consistent with the t-plot analysis. Even though theoretically the BJH method is a desorptive method (i.e., works from higher pressures to lower pressures modelling 'imaginary emptying of a condensed adsorptive'), it can be used for following both the adsorption isotherm downward from high- to low-relative pressure, or the desorption curve. However, pore-size distribution obtained from the desorption curve is limited to ~4–5 nm because of the tensile strength effect (TSE) phenomenon due to the breaking of the meniscus in pores with a diameter around 4 nm or less and hence making application of Kelvin's equation invalid (Groen *et al.* 2003). In this study, we report the pore-size distribution obtained by applying the BJH method from the adsorption isotherm. The limit of the pore diameters that can be evaluated using the BJH theory from the adsorption branch is 1.7 nm because Kelvin's equation becomes invalid in micropores.

Comparison between Pore-Size Distribution from nitrogen adsorption and Mercury Intrusion Porosimetry

Mercury is a strongly non-wetting fluid that does not spontaneously imbibe inside the pores by capillary action. In mercury intrusion porosimetry (MIP), mercury is forced to intrude the pores of porous media by the application of external pressure. The amount of pressure required to intrude a pore is inversely proportional to the size of the pore. The pressure versus intrusion data are inverted to get the pore-size distribution of the sample using the Washburn equation. Current instruments can only go up to 414 MPa (60 000psi), corresponding to a theoretical limit, on the smallest measured pores, of diameter 3.6 nm. However, at this high pressure, blank effects from the heating and compression of the mercury (Sigal 2009), compressing of the rock structure, breaking the particles and opening closed pores (Penumadu and Dean 2000; Bustin *et al.* 2008; Comisky *et al.* 2011) may significantly affect the data. Despite these limitations, the ability of MIP to record macropores with orders of magnitude make it a very useful tool and provide complimentary information of the pores structure compared to gas-adsorption. It should be used in conjunction with gas-adsorption methods to obtain

the most comprehensive description of the pore structure of heterogeneous porous media like shales (Gregg and Sing 1983; Bustin *et al*. 2008). This has been demonstrated by studies on different types of adsorbents (Joyner, Barrett and Skold 1951), charcoal and carbon (Dubinin 1966), clays and soils (Sills, Aylmore and Quirk 1973; Echeverria *et al*. 2008), cements (Diamond 1971), porous silica (Brown and Lard 1974) and shales (Bustin *et al*. 2008).

However, combining information from different measurements should be done with caution and with recognition of the limitations (Rouquerol *et al*. 1994). The reality of the pore structure is very complex and all pore-size distribution data are inverted on the basis of a theoretical equation that requires some simplifying assumptions. For example, one of the key assumptions involved in inverting for PSD from MIP data using the Washburn equation is the value of the contact angle, commonly assumed to be 140°. However, several studies have demonstrated a wide range of contact angles, even between mercury and similar surfaces (Diamond 1970; Gregg and Sing 1983). Penumadu and Dean (2000) reported a five-fold change in the interpreted pore diameter by changing the contact angle from 100° to 170°. Sills *et al.* (1973) demonstrated using a contact angle of 140° for mercury; the MIP pore-size distribution plot is displaced by approximately 20% compared to N_2 and a value of 153° for the mercury contact angle made the plots overlapping. A key factor in the BJH theory is the thickness of the adsorbed layer used to modify Kelvin's equation. The thickness curve should be ideally obtained from N_2 adsorption on a reference solid with the same chemical and surface properties but without pores, which is very difficult to obtain for shales, because of the compositional heterogeneity and presence of clays. One of the several empirical 'universal' thickness equations, each developed for a specific type of material, is used. Kuila *et al.* (2012) demonstrated that using a different thickness equation in the BJH calculation gives an identical distribution shape with the dominant pore modes remaining the same but the differential pore volume for each pore size many differ by up to 60%. The theoretical basis also incorporates simplifying assumptions e.g., cylindrical pore shape in the Washburn and Kelvin equations and assumption of an energetically homogenous surface in the BET theory. Such a theory does not honour the real complexity of the porous media. Hence, the results from any experimental method do not provide the 'true' or absolute value of any pore attribute. Rouquerol *et al*. (1994) recommended treating the results as equivalent 'characteristic' values, depending upon the experiment and theory.

It is also important to understand that different measurement techniques record different aspects of the pore structure. A classic example is provided by the work of Dullien and Dhawan (1974) where they reported different pore-size distributions of the same sandstone sample using optical microscope stereological image analysis on a two-dimensional slice and mercury intrusion measurements. The image analysis resulted in a wide and flat distribution function compared to a narrow, sharp distribution resulting from mercury porosimetry. The modal size is larger in the image-analysis distribution compared to mercury intrusion. The difference in the pore-size distribution was explained in terms of the 'pore-body' measurement, which is revealed in the stereological image analysis measurement compared to the 'pore-throat' measurement in mercury intrusion. A similar phenomenological difference exists between gas-adsorption experiments and MIP. The capillary condensation during adsorption in a complex pore network will be more controlled by the 'pore-body' sizes, while capillary evaporation or pore emptying during desorption will be a more pore-throat controlled phenomenon (Mason 1981; Groen *et al*. 2003) as in MIP intrusion. As per Rouquerol *et al*. (1994)'s recommendation for the multi-techniques characterization of pore space, we should look for systematic agreement, instead of a 'perfect agreement', between parameters provided by different methods. In this paper, we will refer to the pore-size distribution obtained from MIP as 'MIP Pore-throat Size distribution' (MIP-P_tSD), while the pore-size distribution obtained from application of BJH techniques, assuming Harkins-Jura's (HJ) thickness equation, on the adsorption branch of the N_2 isotherm as 'BJH-HJ Pore-body Size distribution' (BJH-HJ-P_bSD).

METHODS AND MATERIALS

Materials

Wyoming montmorillonite (SWy-2) and low-defect Georgia kaolinite (KGa-1b) were obtained from the Source Clay Repository of Clay Mineral Society. These are natural samples and so have some minor contaminants but they are dominated by the specified minerals. These two samples are studied in 'as-received' powdered form to understand the pore structure of these clays in general. However, clays in shales are compacted over the geological history and the physical properties, such as density, porosity, acoustic velocities and permeability change with depth of burial. Mechanical compaction, which is a function of increase in overburden stress, results in a change in the pore structure, exponential decrease in the pore volume with

depth and change in the alignment of the clays. To examine the effect of compaction on the pore structure, Wyoming montmorillonite powder (SWy-2) was artificially compacted using cold pressing techniques to make compacted pellets. The powdered samples were put inside a one-and-half inch cylindrical mould with a piston. The inner surfaces of the barrels were coated with Teflon tapes to prevent sticking of charged clays with the walls during the pressing. This also helps in reducing the friction associated while pushing the sample out of the barrel and made sample recovery simple. Then pressure was applied uniaxially to the mould via the piston at a very slow rate in a cold press. The movement of the piston is controlled by a pump flowing at a constant rate of 0.05 ml/min. Samples were prepared by pressing at different pressures (between 6000–14 000 psi) to obtain pellets with different porosities. The pellets were classified using a clay mineral identifier and the pressure applied, e.g., sample Mont-6K means the pellet is made from Wyoming Montmorillonite by applying 6000 psi of axial load. Rectangular chips (of about 0.5 gm weight) were cut from the pellets using a diamond saw for the gas-adsorption experiments.

Shale samples from different locations with different mineralogy and clay content were also tested to study the effect of clay on the pore-size distribution of shales. The details of the samples are given below and the mineralogy of the samples is shown in Table 1.

1. An illite-rich Cambrian shale sample from Silver Hill, Montana was obtained as ground rock chips from the Clay Mineral society. This particular shale is used as the source for the Clay Mineral Society standard (Imt-2) for illitic clays. The Silver Hill Cambrian shale has dominant silt mineralogy with a significant amount of illitic clays (Table 1).
2. A set of three samples was obtained from the core of the Niobrara Formation in the Berthoud State No. 3 well, Berthoud Field, Larimer County, Colorado (Pollastro 1992; Kuila *et al.* 2012). Niobrara is mainly calcitic with some amounts of illite-smectite clays. The samples are from a depth of 3060 ft (Niobrara Marl B-C), 3150 ft and 3161 ft (Chalk D). The Chalk D samples have negligible organic matter while Marl B-C has a significant amount of organic matter.
3. An assorted set of shale samples, previously studied by Sarker (2010) for elastic and flow properties, were selected. The samples analysed are North Sea Shale, Pierre Shale, Mancos 'B' Shale, Cox Argillite, Middle Bakken Shale and Woodford Shale. Detailed mineralogical, compositional and textural descriptions of the samples are given in Sarker (2010). A sub-sample was used here for the pore-size distribution analysis. Quantitative mineralogical analysis by Quatitative X-Ray Diffraction techniques (QXRD) was repeated to verify the effect of sub-sampling and sample heterogeneity. Except for Pierre Shale and Woodford Shale, the mineralogy is consistent and within the limits of QXRD, as shown in Table 1.

Gas-adsorption experiment

The gas-adsorption experiment using nitrogen as the adsorbent was conducted on a Micromeritics ASAP 2020 surface area analyser, which uses a static volumetric method for measuring the amount of adsorbed gas. Sample preparation was carried out in accordance to ISO 9277: 2010. The samples were degassed at 200°C for at least 12 hours under a vacuum of 10μmHg. This ensures removal of any bound and capillary water adsorbed with the clays, while avoiding irreversible changes to the structure of the clays. The degassing temperature of 200°C is higher than the API (American Petroleum Institute) recommended standard of 110°C for drying the cores. Luffel and Guidry (1992) suggested a heating temperature of 230°F (110°C) to remove the free and clay-bound water. Drits and McCarty (2007) and Srodon and McCarty (2008) reported that smectite and expandable mixed-layered illite-smectite (I-S) clays are capable of retaining significant electrostatic bound water in excess of 200°C. They suggested a temperature of 200°C to be the optimum for degassing clay rich samples. Figure 2 shows the TGA (Thermo-Gravimetric Analysis) and DTG (Differential Thermal Gravimetry) curve for SWy-2 heated at the 5°C/min rate. The secondary peak in the DTG curve indicates removal of the strongly bound water with the clays. We chose a degassing temperature of 200°C based on the TGA data and a recommendation from Srodon and McCarty (2008). The out-gassing rates at the end of this degassing process were <10 μm Hg/min over a 15 minute interval. After degassing, the sample was exposed to nitrogen gas at liquid nitrogen temperature (−197.3°C) at a series of precisely controlled pressures. Free space (dead volume of the tube) determination was done by volumetrically using helium before measurement of the adsorption isotherm. Ultra high-purity grade nitrogen and helium (both 99.99% pure) were used for the experiment.

The compacted SWy-2 clay pellets were cut into small chips for the gas-adsorption analysis. However, the shale samples were crushed to pass through a 40 mesh (<420 μm) before analysis. Most core measurement analyses done on shales are currently performed with a crushed rock sample following

Table 1 Major mineral content of the studied samples. The concentration values reported here are weight per cent normalized to 100% (obtained from QXRD). Following the methods of Środoń *et al.* (2001), quantitative mineral phase compositions were obtained by X-ray diffraction (XRD) analysis of randomly oriented powders spiked with ZnO, (QUANTA^{TM}, Omotoso *et al.* 2006). All dioctahedral Al-rich 2:1 clay minerals (illite, dioctahedral smectite, muscovite and mixed-layered illite-smectite) are quantified together as the illite smectite group mineral (Środoń *et al.* 2001). The Total Organic Carbon (TOC) is measured by the LECO technique. The mineralogy of the samples from Sarker (2010) is shown for reference.

Comment	Qtz	K-spar	Plag	Cal	Sid	Dol.	Pyr	Hal	Opal C / CT	Other min	Sum Non Clay	Kao	Chl	Illite + Smec group	Sum Clay	TOC
Silver Hill Cambrian Shale	7	1	1	1	0	0	0	0	0	0	10	0	1	89	90	N/A
Niobrara Chalk D 3150’	17	0	5	37	0	1	2	0	0	2	65	0	0	35	35	0.42
Niobrara Chalk D 3161’	17	0	3	55	0	4	1	0	0	0	80	0	0	20	20	0.38
Niobrara Marl B-C 3060’	12	0	4	53	0	4	2	0	0	0	76	0	0	24	24	1.86
Middle Bakken	46	4	2	27	0	13	2	0	0	0	94	0	0	6	6	N/A
Middle Bakken (Sarker 2010)	49	5	0	25	0	16	3	0	0	0	98	0	<1	2	2	0.11
Pierre Shale	30	8	11	1	0	4	1	0	0	0	56	0	8	36	44	N/A
Pierre Shale (Sarker 2010)	45	5	15	tr	0	6	2	0	0	0	73	0	3	24	27	18.00
Cox Argillite	24	1	2	24	0	2	1	0	0	0	54	1	3	40	44	N/A
Cox Argillite (Sarker 2010)	26	2	1	21	1	5	1	0	0	0	58	1	2	39	42	0.52
Woodford Shale	63	15	3	0	0	1	1	0	0	0	83	0	0	17	17	N/A
Woodford Shale (Sarker 2010)	5	0	2	0	0	87	1	0	0	3	98	0	0	2	2	1.07
North Sea Shale	7	2	1	0	0	0	1	0	17	0	29	14	0	56	71	N/A
North Sea Shale (Sarker 2010)	9	1	1	2	1	1	1	2	14	0	32	15	0	53	68	0.20
Mancos B shale	43	4	2	7	0	8	1	0	0	0	65	6	0	28	35	N/A
Mancos B shale (Sarker 2010)	39	4	4	9	1	8	2	0	0	0	67	6	0	27	33	1.36

Qtz = Quartz; **K-spar** = K- feldspar; **Plag** = Plagioclase; **Cal** = Total Calcite and Mg-rich Calcite; **Dol** = Dolomite including excess Ca-Dolomite and Ankerite; **Sid** = Siderite; **Pyr** = Prite; **Kao** = total dioctahedral 1:1 layer clay: kaolinite, dickite, nacrite, haloysite; **Chl** = Chlorite; **Illite+Smectite group** = total dioctahedral 2:1 layer clay: illite, mixed-layer illite-smectite, smectite, and mica; **TOC** = Total Organic Carbon (wt%).

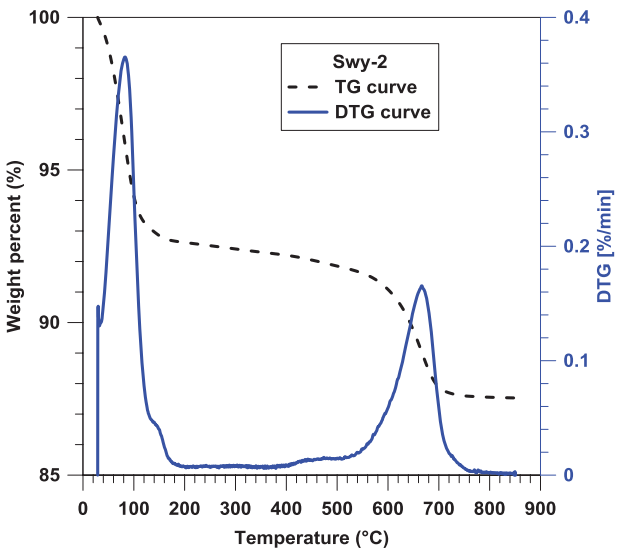

Figure 2 TGA and DTG curves for Mont-Swy2 powders heated from 25–900°C at 5°C/min heating rate. The secondary peak around 160°C in the DTG curve is related to the removal of strong- electrostatically bound water associated with montmorillonite clays. Based on the DTG curve, a degassing temperature of 200°C was chosen for our samples.

the procedure established in the GRI (Gas Research Institute) study on shales (Luffel and Guidry 1992). The rationale behind using the crushed rock methodology is to decrease the path length for the gas to access the entire pore structure and achieve equilibrium within reasonable time. This is particularly important for shales because of their extremely low permeability and also because the low temperature used for the gas-adsorption analysis decreases the gas diffusion rate of the gas through the pores. However, crushed samples will artificially create an external surface area and will show a higher specific surface area than their equivalent intact material, depending upon the particle size distribution of the crushed powder. To understand the effect of crushing, a particle size analysis using laser profile size analysis was done on the 'as-received' powdered source clay SWy-2, suspended in isopropyl alcohol. Assuming spherical particles with no porosity and a grain density of 2.85 g/cc for dehydrated smectites, the calculated specific surface area of the powder is equal to 0.0646 m^2/g (Fig. 3), which is an order of magnitude lower than the measured specific surface area obtained of the shale samples. Hence, we concluded that crushing will not significantly affect the measured specific surface area of the samples. Each shale sample was ground to <425 μm (<40 mesh) powder, homogenized and spilt using a Riffle splitter to obtain the mineralogical and chemically equivalent portions for QRXD and adsorption analysis.

Mercury intrusion capillary pressure experiment

Mercury intrusion experiments were carried out on the 'as-received' clay powder SWy-2 and two clay compacted samples using Micromeritics AutoPore IV 9500. The pressure range applied was 0.14–420 MPa with an equivalent pore-size range of 3.6–10^4 nm. The samples are degassed at 50 μmHg evacuation pressure for at least 30 minutes and 3–5 gm of the samples were used. Every pressure point was

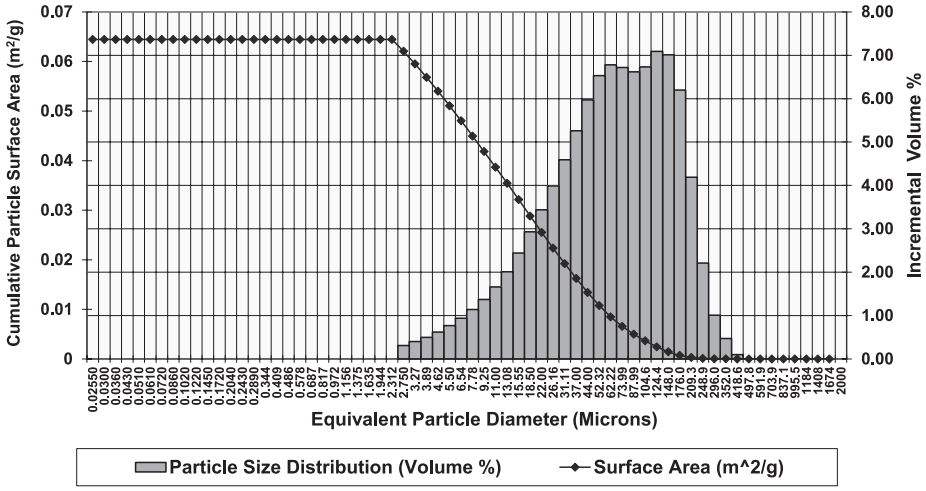

Figure 3 Incremental volume percent particle size distribution (histogram) of SWy-2 measured by laser profile size analysis on crushed powder suspended in isopropyl alcohol. The cumulative external specific surface area (curve line with dots) of the powder is calculated assuming spherical grains with a grain density of 2.85 g/cm^3. Note that the reported particle size distribution is that of a crushed powder and not the actual grain size distribution of the clay.

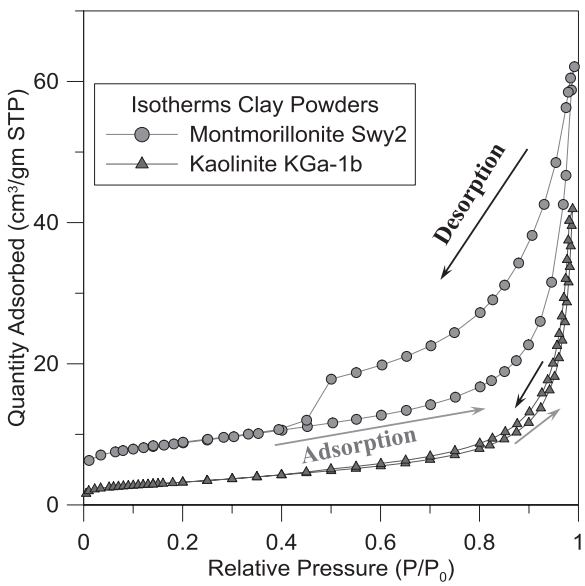

Figure 4 Adsorption-desorption isotherms of N_2 at liquid N_2 (−197.3°C) temperature of 'as-received' powders of Wyoming Montmorillonite SWy-2 and Kaolinite KGa-1b. The isotherm shapes indicate that the kaolinite powders are mostly macroporous, with negligible or non-existent micropores and mesopores. Montmorillonite powders show a presence of significant volumes of micropores, mesopores and macropores. (See text for detailed description.)

equilibrated below the 0.001 μL/g/s intrusion rate. The MIP data on the shale samples have been previously measured (Sarker 2010). The analysis was done commercially from outside vendors on whole core samples and the reported MIP data are conformance-corrected. (Rituparna Sarker, pers. comm.).

RESULTS

Adsorption isotherms

Figure 4 shows the adsorption-desorption isotherms of N_2 at liquid N_2 (−197.3°C) temperature of the 'as-received' powders of Wyoming Montmorillonite SWy-2 and Kaolinite KGa-1b. The shape of the isotherm gives a qualitative assessment of the porous structure of the materials. The isotherms show a marked difference in shape. Uncompacted kaolinite shows an almost reversible Type II nitrogen isotherm. The isotherm shape indicates that kaolinite is dominantly macroporous and micro-mesopores are absent. The hysteresis is extremely narrow indicating presence of fine macropores. The amount adsorbed at very low-relative pressure (P/Po < 0.01) is very low indicating that Kaolinite (KGa-1b) has negligible or non-existent micropores.

The Wyoming Montmorillonite SWy-2 powder shows a significant hysteresis pattern but does not show a plateau at high P/Po like the Type IV isotherm. Rouquerol *et al.* (1998) preferred using the designation Type IIB for such an isotherm. Such an isotherm shape indicates that the material contains both mesopores, which is responsible for the hysteresis and macropores, which results in the absence of the plateau like mesoporous Type IV isotherms and having steep slopes in the relative pressure range of 0.98–1.00. The H3 hysteresis pattern indicates presence of slit-like pores. The isotherms also show the 'forced closure' of the desorption branch at 0.35 < P/Po < 0.55 due to the 'tensile strength effect'. This indicates that SWy-2 has a significantly larger amount of small mesopores with diameter <4 nm (Groen *et al.* 2003). The volume uptake at P/Po near 1.0 indicates the total porosity of materials up to the ~200 nm pore-size range. Montmorillonite powders have larger pore volumes in the 200 nm pore-size range compared to the kaolinite powders. Furthermore, they have more micropores than kaolinite, as indicated by a larger adsorbed volume at very low-relative pressure (P/Po < 0.01). Quantitative estimates of the micropore volume are obtained by t-plots as will be discussed later.

The natural shales show a wide variety of pore structure based on their isotherm shapes (Fig. 5). Niobrara (Chalk D and Marl B-C), Pierre Shale and Cox Argillite show Type IIB isotherm shapes similar to SWy-2. The Silver Hill Cambrian Shale shows a close to Type IV isotherm shape (no steep slopes in the relative pressure range of 0.98–1.00) with a H4 hysteresis pattern indicating that this sample has micropores and mesopores and no significant amount of macropores. Mancos B Shale, Woodford Shale and Middle Bakken show Type II isotherms with a very low amount of gas adsorbed compared to other shales and a lower hysteresis indicating a dominantly macroporous nature of the samples. The North Sea Shale shows an extremely low adsorbed volume at low- and intermediate-relative pressure but a high adsorbed volume and a prominent hysteresis at higher relative pressure. The North Sea Shale has no micropores and fine mesopores but has a significant volume of larger mesopores and macropores.

Specific surface area and pore volumes

We compare here specific surface areas calculated from the adsorption isotherms using the modified BET theory and t-plots. The comparison of the modified BET specific surface area and the t-plot open specific surface area calculations are given in Table 2. Kaolinite, Niobrara Marl B-, North Sea

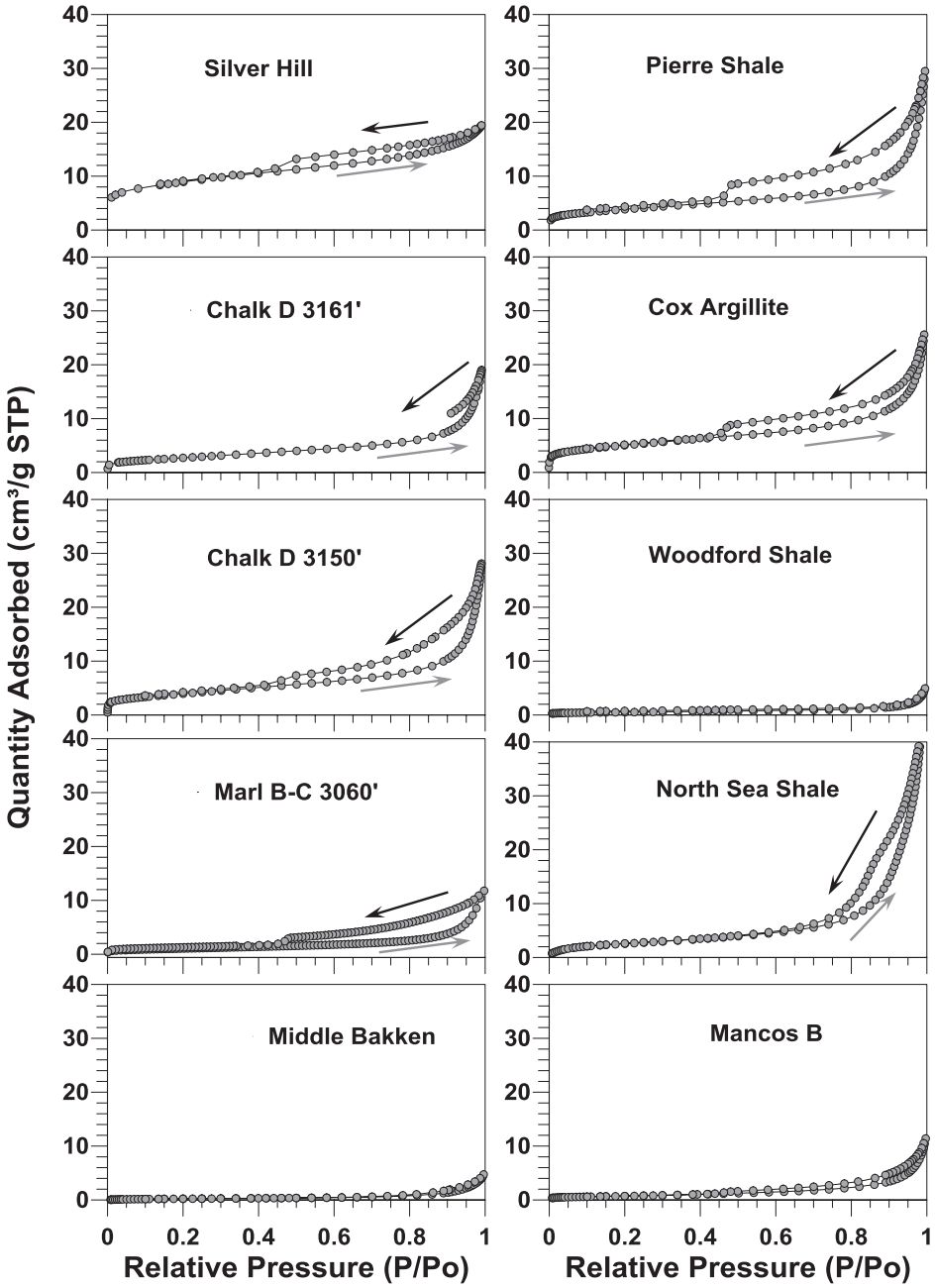

Figure 5 Adsorption-desorption isotherms of N_2 at liquid N_2 (−197.3°C) temperature of the natural shale samples used in this study. Based on the isotherm shapes, the nature of the pore structure for the different samples is inferred. The Niobrara (Chalk D and Marl B-C), Pierre Shale and Cox Argillite show presence of fine mesopores and larger mesopores and macropores. The Silver Hill Shale is dominated by micropores and mesopores with no macropores. The Middle Bakken, Woodford and Mancos B Shales are dominantly macroporous. The North Sea Shale has larger mesopores and micropores but no micropores and fine mesopores (see text for details). Note that Chalk D 3161' does not have the desorption branch measured due to power outrage and a technical problem during analysis.

Shale, Mancos B shale and Middle Bakken show a similar specific surface area obtained from the two methods. Montmorillonite powder SWy-2, pellets made from SWy-2, Silver Hill Cambrian Shale, Chalk D, Pierre Shale, Woodford Shale and Cox Argillite show significant differences between the two specific surface areas. The differences in these values can be correlated to the surface area associated with the micropores (pores less than 2 nm diameter) since the 'open specific surface

Table 2 Comparison of the modified BET specific surface area, the open specific surface area obtained from the t-plot and the micropore specific surface area of the samples based on N_2 adsorption isotherms. The uncertainty estimate is only calculated from the misfit of the regression fit to the actual data point. Other experimental uncertainties are not evaluated.

Sample	Modified BET Specific Surface Area (m^2/g)	Open Specific Surface Area by t-plot (m^2/g)	% Specific surface area contributed by micropores (%)
'As-received' Source Clays (powders)			
KGa-1b	11.49 ± 0.02	11.40 ± 0.04	0.78%
SWy-2	31.13 ± 0.16	19.68 ± 0.24	36.78%
Pellets made from SWy-2			
Mont-4K	31.81 ± 0.16	18.73 ± 0.34	41.12%
Mont-6K	30.26 ± 0.14	17.71 ± 0.22	41.47%
Mont-8K	31.55 ± 0.15	18.50 ± 0.40	41.36%
Mont-10K	29.75 ± 0.13	18.26 ± 0.41	38.62%
Natural Shale Samples			
Silver Hill Cambrian Shale	31.57 ± 0.18	20.26 ± 0.44	35.83%
Niobrara Chalk D 3161′	9.91 ± 0.01	7.41 ± 0.07	25.23%
Niobrara Chalk D 3151′	14.29 ± 0.02	9.13 ± 0.02	36.11%
Niobrara Marl B-C 3060′	3.89 ± 0.01	3.83 ± 0.01	1.57%
Middle Bakken Shale	0.98 ± 0.003	1.02 ± 0.002	–
Pierre Shale	13.93 ± 0.02	9.17 ± 0.02	34.17%
Cox Argillite	18.09 ± 0.03	10.34 ± 0.04	42.84%
Woodford Shale	1.93 ± 0.01	1.61 ± 0.02	16.58%
North Sea Shale	9.60 ± 0.03	10.11 ± 0.03	–
Mancos B Shale	2.82 ± 0.03	2.82 ± 0.08	–

Table 3 Comparison of the total and micropore volumes of the samples determined by N_2 adsorption data by t-plot and MIP.

Sample	Total Pore Volume N2 (cm^3/g)	Total Pore Volume MIP (cm^3/g)	Micropore volume by t-plot (cm^3/g)	% Micropore on N_2 pore volume
KGa-1b	0.049	–	0.000	0.00%
SWy-2	0.068	0.517	0.005	7.35%
Mont-4K	0.063	0.206	0.006	9.52%
Mont-6K	0.060	–	0.005	8.33%
Mont-8K	0.062	0.170	0.006	9.68%
Mont-10K	0.056	0.129	0.005	8.93%
Silver Hill Cambrian Shale	0.030	–	0.005	16.67%
Niobrara Chalk D 3161′	0.029	–	0.001	0.34%
Niobrara Chalk D 3150′	0.043	–	0.003	6.76%
Niobrara Marl B-C 3060′	0.017	–	0.000	—
Middle Bakken Shale	0.006	0.009	0.000	—
Pierre Shale	0.040	0.074*	0.002	6.05%
Cox Argillite	0.036	0.061	0.004	10.76%
Woodford Shale	0.006	0.002*	0.000	–
North Sea Shale	0.062	0.176	0.000	–
Mancos B Shale	0.014	0.026	0.000	–

* Sub-samples used for gas-adsorption and MIP have different mineralogy (see Table 1).

area' obtained from the t-plot typically provides the specific surface area from mesopores, macropores and an external specific surface area (the total specific surface area excluding the specific surface area of micropores). Table 3 shows the comparison of the total pore volume obtained from the N_2 adsorption isotherm, the micropore volume obtained by the t-plot method and the mercury intrusion total pore volume. Kaolinite, Niobrara Marl B-C, Middle Bakken, North

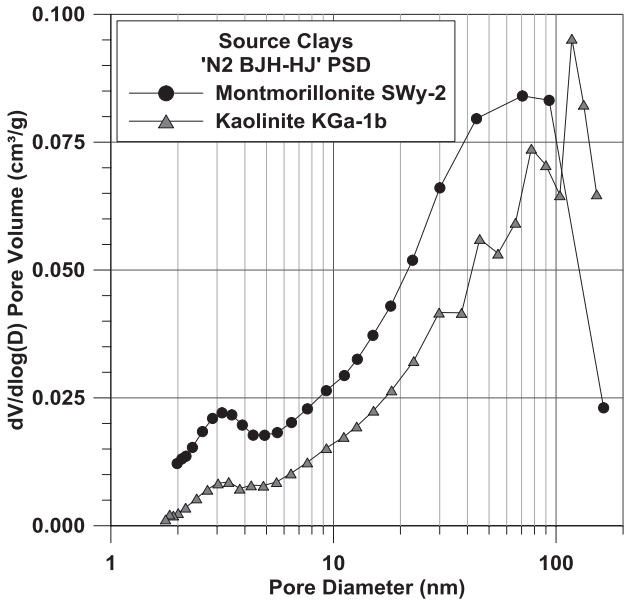

Figure 6 BJH-HJ P_bSD of 'as-received' source clay powders: Montmorillonite (Swy2) and Kaolinite (KGa-1b) obtained from the N_2 adsorption isotherm. Swy2 has bimodal distribution with a major peak between 60–100 nm with a minor peak around 3–4 nm. KGa-1b shows unimodal distribution with a peak around 100 m.

Sea Shale and Mancos Shale show no or negligible micropore (smaller than 2 nm diameter) volumes. Silver Hill Cambrian Shale shows the highest proportion of micropores (16.67%) of the total N_2 adsorption measured porosity. The MIP pore volume shows a higher value than the N_2 adsorbed pore volume. This difference can be attributed to the presence of macropores that the N_2 adsorption method cannot measure. Another important observation is that the micropore volumes per unit gm of the samples are almost constant for all the montmorillonite clay samples, both the pellets and powder. Note that the specific surface area contributed by the micropores to the total specific surface area is more significant compared to the micropore volume contribution to total pore volume (Tables 2 and 3).

Pore-size distributions

Source clays: Fig. 6 shows the BJH-HJ P_bSD (partial volume V of each pore diameter D) obtained from inverting the adsorption branch of the isotherm for the powdered source clay samples. The parameter dV/d (logD) is used because the area under the curve between any two pore diameters can be used to assess the partial porosity for each pore diameter range. For Montmorillonite powder Swy2, the distribution is bimodal with a major peak between 60–100 nm and a minor but prominent peak around 3–4 nm. Kaolinite KGa-1b shows mostly a unimodal BJH-HJ P_bSD with a peak around 100 nm.

Compaction: Fig. 7(a) shows the BJH-HJ P_bSD of the compacted pellets made from SWy-2. The compacted pellets show a similar bimodal distribution as the powder SWy-2. The pore

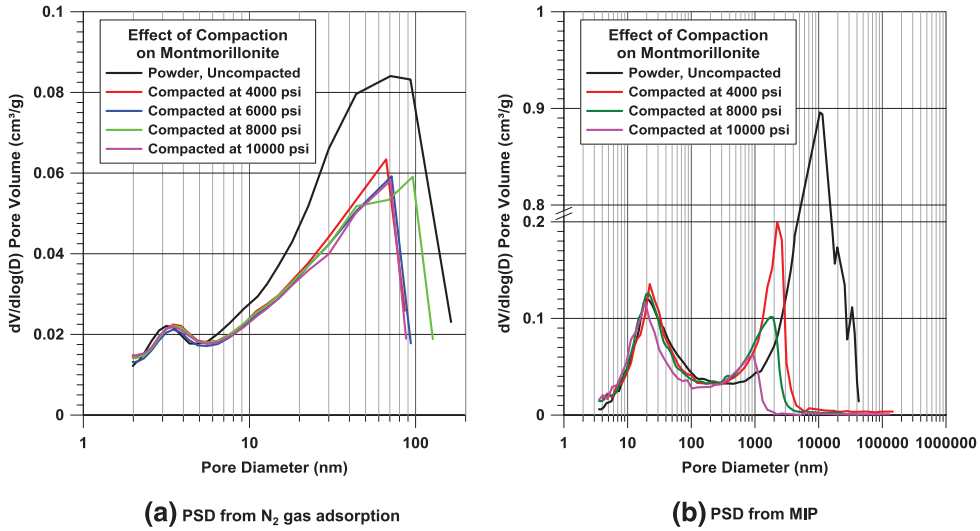

Figure 7 (A) BJH-HJ P_bSD of compacted clay pellets. The samples show similar consistent bimodal distributions as SWy-2. The pore volume around the 3–4 nm peak remains unchanged with the applied axial load. There is a significant decrease in pore volume in the compacted pellets around the 60 nm peak with the greatest decrease between Swy2 powder and pellets compacted at 4000 psi. (B) Pore (throat)-size distribution of 'as-received' SWy-2 compacted clay pellets Mont-4K, Mont 8K and Mont-10K obtained from MIP. Note that the y-axis is broken to show the large amount of pores in the powders. Bimodal distribution with modes at 20 nm and around 1000–2000 nm is observed for the pellets. The pore volume around 1000–2000 nm decreases with compaction. Also the mode decreases from 2000 nm in Mont-4k to 1000 nm in Mont-10K.

volume around the 3–4 nm peak does not change with the applied axial load. There is a significant decrease in pore volume in the compacted pellets around the 60 nm peak with the greatest decrease seen between Swy2 powder and pellets compacted at 4000 psi (Mont-4K). With further compaction there is a slight decrease in porosity in the 60 nm range. The distribution patterns are consistent for all the compacted pellets. Figure 7(b) shows the MIP-P_tSD on Mont-4K, Mont-8K and Mont-10K. It shows a dominant bimodal pore-throat size distribution with modes at 20nm and around 1000–2000 nm for the compacted pellets. The porosity associated with the 20 nm mode remains constant for all the samples, except for Mont-10K. The total pore volume in this pore range and the modal size are lowest in the highest compacted pellet. The porosity around 1000–2000 nm decreases with compaction; Mont-4K has the largest pore volume followed by Mont-8K and the lowest is in Mont-10K. Also, the mode decreases from 2000 nm in Mont-4k to 1000 nm in Mont-10K.

Natural shales: Fig. 8 shows the BJH-HJ P_bSD of all the natural samples. The previously measured MIP data on some of the shales (Sarker 2010) show similar pore modes (within 10–20 nm) as compared to BJH-HJ P_bSD, except for Woodford Shale. This mismatch can be related to the sub-sampling heterogeneity, as indicated in the difference in mineralogy (Table 1). The Silver Hill Cambrian Shale is dominated by fine mesopores (with diameter around 2–3 nm). The North Sea Shale has the highest porosity and it does not show any fine mesopores and the dominant pores are large mesopores (20–30 nm pore size) and macropores. MIP P_tSD have lower modal pore-size with sharp narrow peaks as compared to BJH-HJ P_bSD, which have higher modal pore-sizes with broader peak. Middle Bakken and Woodford Shale show very little porosity with mostly larger mesopores (30–50 nm) and macropores.

DISCUSSION

Comparison of PSD from MIP and N_2

BJH-HJ P_bSD and MIP P_tSD provide complimentary information on the pore structure in clays and shales. The significant differences between the two distributions are that BJH-HJ P_bSD tends to be broader and the modes are at higher pore sizes compared to MIP P_tSD (Figs 8 and 9). The difference in the distribution shapes is due to the fact that the adsorption process gives a pore-body distribution (Mason 1982; Groen *et al.* 2003) wherease MIP is essentially a pore-throat measurement. The difference in the modal size between the pore body distribution and the pore throat distribution ranges from 10–20 nm in shales (Fig. 8) and from 70–80 nm in pure clays (Fig. 9). The difference in shapes of these two distributions was similar as illustrated by Dullien and Dhawan (1974). Overall the total porosity obtained by N_2 is systematically lower than MIP for all the samples (Table 3). The MIP distribution curves indicate that the largest pore-throat size of the shale samples is less than 200 nm (except for Pierre Shale, Fig. 8), however the N_2 isotherm shape and BJH-HJ P_bSD suggest the presence of larger macropore bodies (<200 nm) in all of the shale samples.

Claymicrostructure

The measured specific surface area of the source clays SWy-2 and KGa-1b (31.13 and 11.49 m^2/g, respectively) is in good agreement with the reported values by the Clay Mineral Society (31.82 and 10.4 m^2/g, respectively) (http://www.clays.org/SOURCE%20CLAYS/SCdata.html). The pore volumes, obtained both from N_2 and MIP, are highest in the powder and decrease with compaction (Table 3, Fig. 9). The presence of micropores agrees well with the reported micropore volume in homoionic pure Wyoming Montmorillonite (Rutherford *et al.* 1997). The reported micropore volumes, between 0.004–0.008 cc/g for different exchange cations, are in the range of our measured micropore volumes for natural untreated montmorillonite (0.006 cm^3/g).

BJH-HJ P_bSD and MIP P_tSD suggest a multiple scale of porosity associated with smectitic clays. Aylmore and Quirk (1971), Cases *et al.* (1992), Neaman *et al.* (2003) and Jullien *et al.* (2005) reported a multiscale structure or building blocks within the clay structure. Our measurements show that such building blocks are associated with specific pore sizes. Based on our pore-size distribution results (Fig. 9), we identify the following porosities associated with the different multiscale structures of clay minerals and their aggregates:

1. 'Intra-tachoid' porosity (fine mesopores): pores with diameter 3 nm are correlated with the pore spaces within tachoids formed by turbostactic stacking of clay elementary units.
2. 'Intertactoid' or 'intra-aggregate' porosity (large mesopores and fine macropores): pores with diameter around 50–100 nm account for the porosity within 'aggregates' formed by stacking of the tachoids. MIP P_tSD suggests that the pore throats associated with these pores have a modal size of about 20–25 nm.

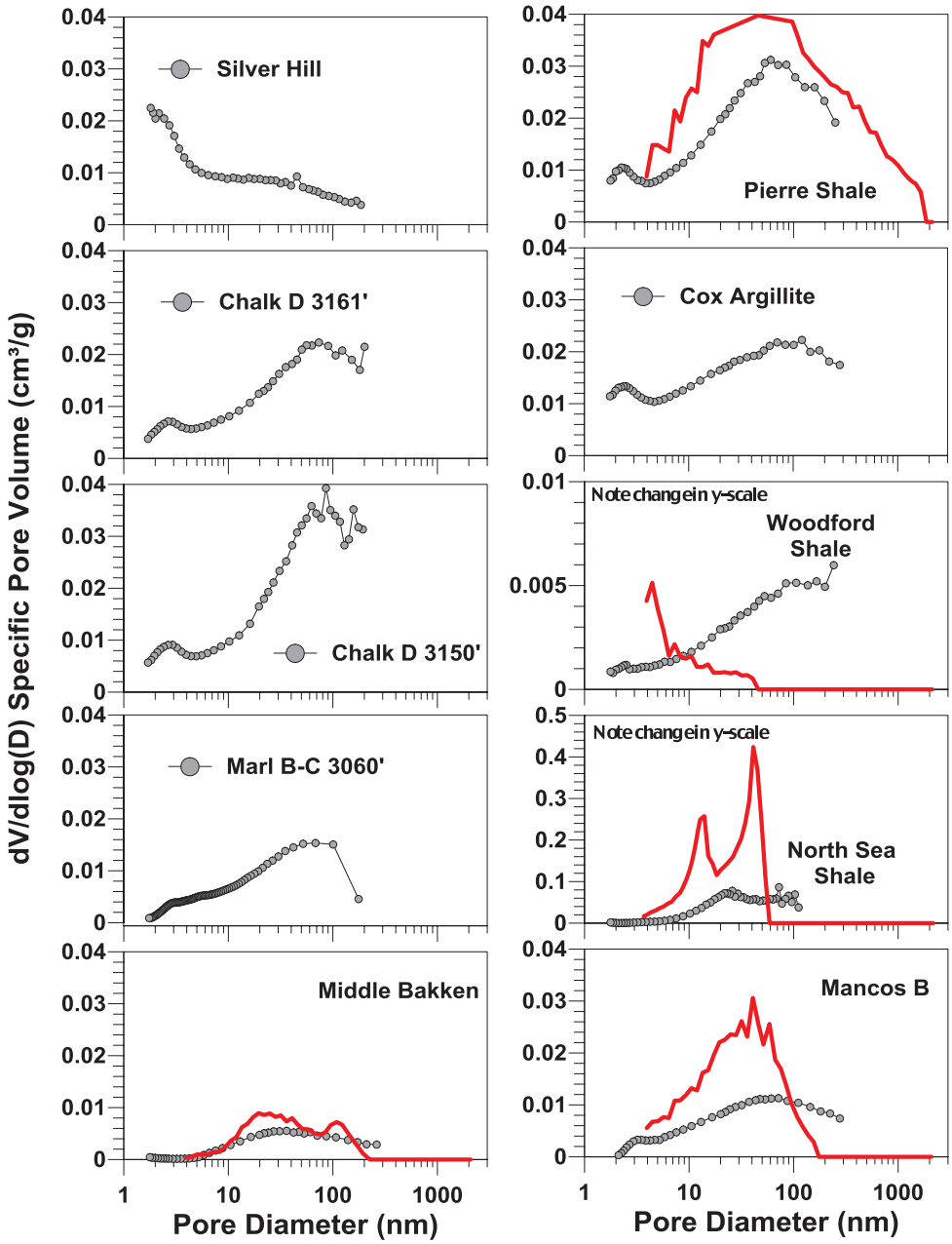

Figure 8 Pore-size distribution of the natural shale samples obtained from the N_2 adsorption isotherm (black line with grey points) and MIP (red line). The limit of PSD is up to 1.7 nm because Kelvin's equation is not valid for micropores. The Silver Hill Cambrian Shale is dominated by fine mesopores (with diameter around 2–3 nm). Niobrara Chalk D, Pierre Shale, Cox Argillite and Mancos B Shale show similar bimodal BJH-HJ P_bSD, like the montmorillonite with a very prominent peak at 3 nm. The North Sea Shale has the highest porosity (note the y-axis value different from other plots) and it does not show any fine mesopores and the dominant pores are large mesopores and macropores. Middle Bakken and Woodford Shale have very low porosity in 1.7–200 nm. Note that MIP P_bSD is not available (N/A) for some samples since MIP was not run on those specific samples.

3. 'Inter-aggregate' porosity (micron size range): the mode around 2000 nm obtained from the MIP data can be correlated with the pore throats of the pores between the aggregates of clays.

Compaction has the biggest effect on the 'inter-aggregate' macropores. Better alignment of clay particles and compaction of pores with applied stress decreases the 'inter-aggregate' pores and also shifts their modal pore size to lower values. The

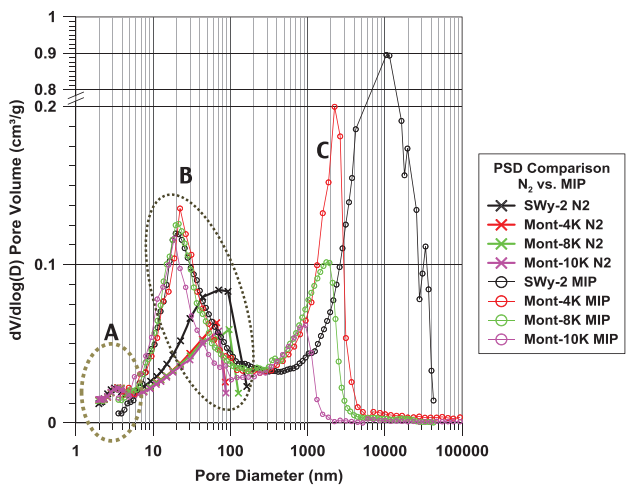

Figure 9 Comparison of BJH-HJ P_bSD and MIP- P_tSD for SWy-2, Mont-4K, Mont-8K and Mont-10K. A mode is detected at 3–4 nm in N_2 and a second mode around 60–70 nm, which is also observed in MIP experiments, although the position of the peaks does not match precisely. MIP suggests a lower pore diameter (20 nm). The three modes observed in these distributions can be correlated with multi-scale porosity associated with clay structures especially montmorillonite. Mode A corresponds to 'intra-tachoid' pores, Mode B corresponds to 'intertactoid' or 'intra-aggregate' mesopores and Mode C corresponds to macropores between aggregates.

'intra-aggregate' porosity is lesser affected from compaction, while 'intra-tachoid' (or 'intertachoid') porosity (pores with 3–4 nm diameter) does not change with compaction. The fine 'intra-tachoid' mesopores are shielded from compaction because of their small pore sizes and stronger molecular forces that prevail in these pores. Equivalence can be drawn from studies of the collapse strength of cylindrical pipes with constant pipe-wall thicknesses, which suggest that the elastic buckling collapse pressure of such a pipe is inversely proportional to the cube of their diameter (Sharp 1981). The small diameter of the pores increases their collapse strength that shields them from compaction. These pores are in a size range where molecular forces dominate, which also helps withstand overburden pressures.

However, the compaction experiments on dry powders are very different from the natural compaction process that occurs in shale. Natural clays and shales have water and low permeability and the artificial experiment carried out in this study has no water. The pore-size distribution of the several naturally compacted shales shows a similar pore structure as we obtained from the clay experiment (Fig. 10). The abundance of 3 nm pore sizes (proportional peak area in dV/d(logD) plot) correlates with the amount of illite-smectite clays present in the samples. In the shale samples, the 3 nm 'intra-tachoids' pores are also shielded from the natural compaction process. We will later discuss the importance of our assessment of incompressible 3 nm sized pores for building a clay mineral modulus.

Compositional controls on a shale-pore structure

We now assess the correlation between pore structure and composition in natural shales. BJH-HJ P_bSD, MIP P_tSD and mineralogy results for the different samples are summarized in Table 4. All the samples with a significant amount of the illite-smectite group of clays show a prominent peak around 3 nm in BJH-HJ P_bSD (Fig. 10), similar to the SWy-2 powders and pellets. The SEM image of Cox Argillite (Sarker 2010) reveals a clay dominated continuous microstructure with distributed angular detrital grains, such as dolomite and quartz (Fig. 11a). The continuous clay matrix controls the main pore-size distribution of these samples. The pore volume of these 3 nm pores(body) in the natural shales increases with increases of the illite-smectite group of clays (Fig 10). The North Sea Shale sample, with about 14% Opal C/CT, shows a slight amount of the 3 nm pore(body) sizes in spite of having a 56% illite-smectite group of clays. The dominance of 10–20 nm pores correlates well with the reported presence of pores of 10 nm diameter in opal (Feoktistov *et al.* 2001). The Niobrara Marl B-C sample, having 24% I-S clay, shows fewer 3nm pores compared to Chalk D 3161' with 20% I-S clays. This is due to the presence of organic matter acting as a pore-blocking material within the clay package, reducing the fine mesopore volumes. Kuila *et al.* (2012) demonstrated that organic materials, depending upon their maturity stage, can act as a pore blocking material within a clay matrix. Figure 11(b) shows a SEM image from the Middle Bakken sample demonstrating extensive calcite cementation in the samples destroying porosity. Hence the Middle Bakken Shale shows very low porosity with mostly large mesopores and macropores.

Implication for rock-physics modelling

The partitioning of total pore volume into pore sizes of different order in illite-smectite clays in the presence of 3 nm intra-tachoids porosity, which is shielded from compaction, has implications in rock-physics modelling of shale. The building end-member of many shale rock-physics models is the clay-water composite. Hornby *et al.* 1994 used a combined self-consistent approximation and differential effective medium

Table 4 Summary of the pore-space characterization results from gas-adsorption and mercury injection and mineralogy. Note that information on MIP P_tSD is not available (N/A) for some samples since MIP was not run on those specific samples.

		N_2 Gas Adsorption			MIP
Sample	Composition	Micro pores present?	Macro pores present?	BJH-HJ P_bSD	MIP P_tSD Modes
KGa-1b	Kaolinite powder	No	Yes	Unimodal: 100 nm	N/A
SWy-2	Montmorillonite powder	Yes	Yes	Bimodal: 3; 70 nm	2 modes: 20 nm; 10000 nm
Mont-4K	Mont at 4000 psi	Yes	Yes	Bimodal: 3; 65 nm	2 modes: 20 nm; 2500 nm
Mont-6K	Mont at 6000 psi	Yes	Yes	Bimodal: 3; 70 nm	N/A
Mont-8K	Mont at 8kpsi	Yes	Yes	Bimodal: 3; 90 nm	2 modes: 20 nm; 2000 nm
Mont-10K	Mont at 10kpsi	Yes	Yes	Bimodal: 3; 65 nm	2 modes: 20 nm; 1000 nm
Silver Hill Cambrian Shale	89% I-S clays	Yes	Yes	Unimodal, 2–3 nm	N/A
Niobrara Marl BC	I-S 24%; Cal 53%; TOC 1.86	No	Yes	Bimodal: very diffuse 3 nm peak 90 nm	N/A
Niobrara Chalk D 3150′	I-S 35%, Cal 37%; TOC 0.42	Yes	Yes	Bimodal; prominent 3 nm; 80–90 nm	N/A
Niobrara Chalk D 3161′	I-S 20%, Cal 55%; TOC 0.38	Yes	Yes	Bimodal; prominent 3 nm; 80–90 nm	N/A
Middle Bakken Shale	Qtz 46%; Cal 27%; I-S 6%	No	Yes	Broad unimodal; 60 nm	Broad Bimodal: 20 nm; 100 nm
Pierre Shale	Qtz 30%; I-S 36%	Yes	Yes	Bimodal; prominent 3 nm; 100 nm	Broad Unimodal: 100 nm eterogeneous sub-sample)
Cox Argillite	Qtz 24%; Cal 24% I-S 40%	Yes	Yes	Bimodal; prominent 3 nm; 150 nm	N/A
Woodford Shale	Qtz 63%; I-S 17%	No	Yes	Unimodal : 200 nm	Unimodal: 7 nm (heterogeneous sub-sample)
North Sea Shale	I-S 56%, Qtz 7%; Opal C/CT 17%	No	Yes	Unimodal no pore below 10 nm: 300 nm mode	Bimodal: 20 nm 60nm
Mancos B Shale	Qtz 43%; I-S clay 28%	No	Yes	Bimodal: Diffuse 3 nm, 90–100 nm	Unimodal 60 nm

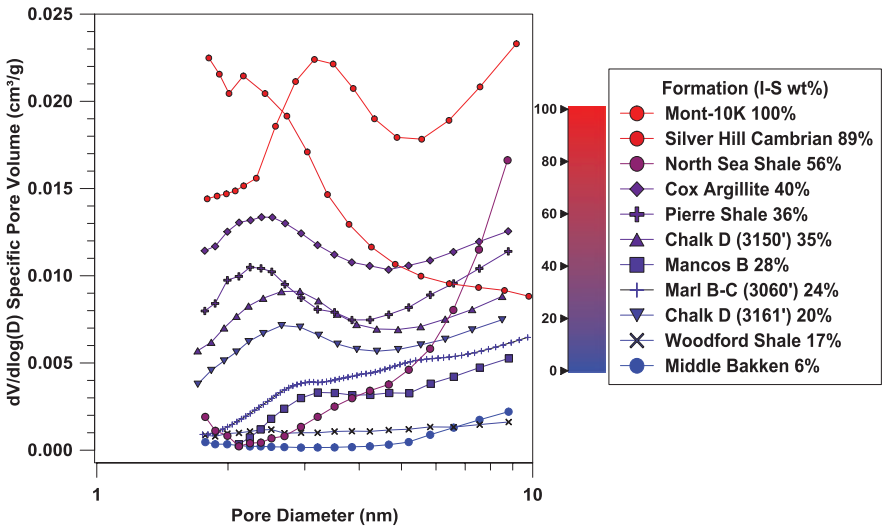

Figure 10 BJH-HJ P_bSD of the natural shale samples up to 10 nm pore diameter. The color bar indicate amount of I-S clay in the sample, red colour indicating highest clay content. The legend shows the illite-smectite (I-S) group clay content in wt.% (or 'intertachoid'). The area under the curve with a particular size range is proportional to the absolute pore volume for that size range. Samples with lowest clay content (blue) do not have a 3 nm pore-body distribution peak and the 3 nm pores become increasingly abundant with increasing clay content. The North Sea Shale sample does not show any 3 nm porosity in spite of having 56% of I-S clays.

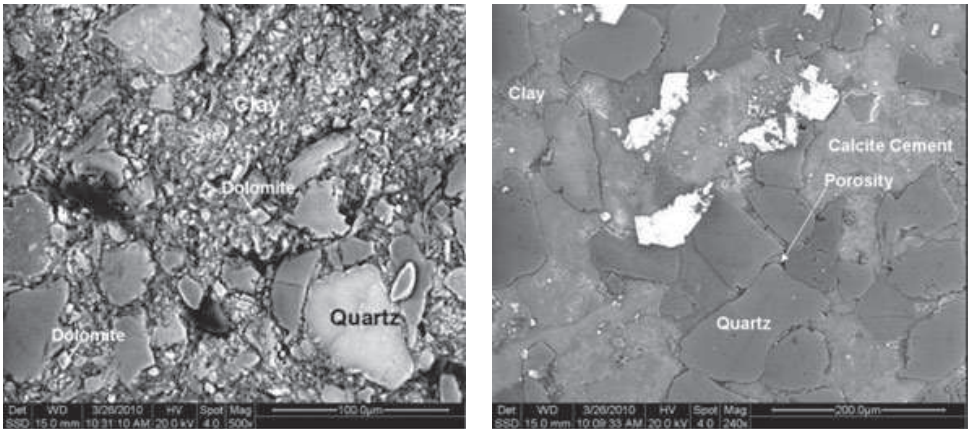

(a) SEM backscatter image of the Cox Argillite (image from Sarker, 2010)

(b) SEM backscatter thim section image of the Middle Bakken (image from Sarker, 2010)

Figure 11 (a) SEM backscatter image of the Cox Argillite (Sarker 2010). The rock shows a clay dominated continuous microstructure with distributed angular detrital grains, such as dolomite and quartz. (b) SEM backscatter thin section image from the Middle Bakken sample (Sarker 2010). The microstructure in this sample is controlled by extensive calcite cementation destroying porosity.

(SCA-DEM) approach to model the clay-water composite, where a biconnected medium of the clay-water medium is initially formed using SCA, which is later adjusted to the 'target porosity' using DEM. However, the porosity of this clay-water composite is not exactly known. Our assessment of incompressible 3 nm sized pores associated with the illite-smectite group of clays provides an important building block for their mineral modulus. The tachoids of clays can be imagined as the basic elastic end member of shale rock. Figure 12 shows the plot pore volume between 2–5 nm pore diameter obtained from gas-adsorption with respect to the illite-smectite clay content (wt.%) for all the studied natural shale samples (except North Sea Shale). The linear fit, extrapolated to 100% illite-smectite clay content, gives a value

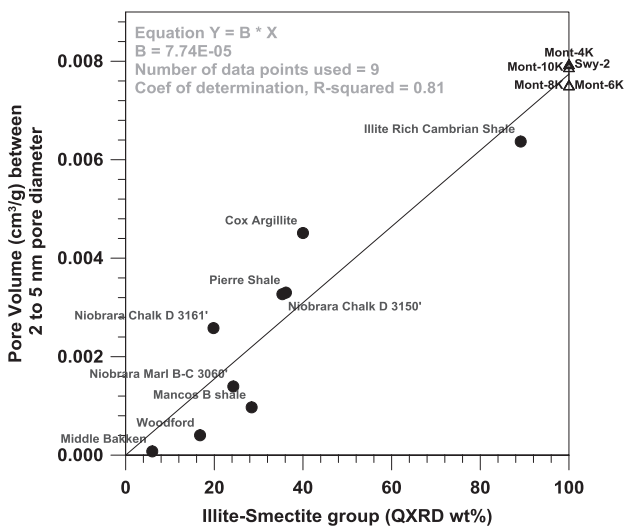

Figure 12 Pore volumes between 2–5 nm diameter obtained from N_2 gas-adsorption are plotted as a function of the I-S clay content (wt.%) for the natural shale samples except for the North Sea Shale (filled circles). A linear trend with zero intercept (equation y = bx) is fitted to the data points. Note that the result from the pure montmorillonite (open triangles) is not used in the regression and is shown only for reference.

of 0.0077 cm^3/g for the intra-tachoid pore volume of clays. The extrapolated value from natural shales coincides with the pore volume obtained for the pure clays. A pore volume of 0.0077 cm^3/g will translate into a porosity value of 2.1% assuming an anhydrous grain density of 2.85 g/cm^3 for the illite-smectite group. Hence our building block for the illite-smectite mineral modulus can be thought of as clay tachoids with 2.1% porosity. Neaman *et al.* (2003) explained the possible arrangement of these pores in tactoids as slit-shaped porosity at the egdes of turbostatically arranged unit cells or as rectangle-shaped porosity formed by initial arrangement of the interlayers. Using a Reuss average between the dry clay modulus of 55 GPa from Katahara (1996) and water (2.2 GPa), we derived a bulk modulus of the smectite clay-water composite as 36 GPa. This should form a fundamental mineral end-member for illite-smectite clay. The presence of 'inter-aggregate' pores formed by the arrangement of tachoids within a single aggregate of clay will also reduce the modulus of the clay-water composite.

CONCLUSIONS

Conclusions from the performed experiments on clays and natural shales using a combined pore-size distribution analysis from the N_2 gas-adsorption technique and MIP can be summarized as follows:

- The illite-smetite group of clays shows multiple scales of pore structures:
  1. 'Intra-tachoid' pores (~3 nm) formed by stacking of elementary unit cells in tachoids
  2. 'Intra-aggregate' pores (20–100 nm) formed by stacking of tachoids in an aggregate and
  3. Larger macropores (> 1000 nm) between the aggregates.
- Montmorillonite has micropores and fine mesopores with a characteristic pore size of 3 nm that is missing in kaolinite.
- Presence of micropores/fine mesopores in natural shales can be correlated with the dominance of the illite-smectite type of clays in the rock.
- Compaction of montmorillonite shows:
  1. Decrease in pore volume and reduction of pore size in the 'inter-aggregate' macropores
  2. Some reduction in pore volume of the 'intra-aggregate' mesopores and fine macropores
  3. No change of 'inter-tachoid' micropores and fine mesopores.
- The incompressible 3 nm pores associated with illite-smectite clay tachoids can be used as a building block for the mineral modulus of illite-smectite clays in rock-physics modelling of shales. The mineral modulus of the illite-smectite clay-water composite with approximately 2.1% inter-tachoid porosity is estimated to be 36 GPa.

ACKNOWLEDGEMENTS

We will like to acknowledge Dr. Douglas K. McCarty, Dr. Timothy Fischer, Prince Ezebuiro, Ferell Garner and Steve Yurchick from Chevron ETC, for allowing to use their facility and their kind help in obtaining the QXRD and MIP measurements on the samples. We will also like to thank Dr. Rituparna Sarker for providing the MIP data for the shale samples. The authors gratefully acknowledge the OCLASSH consortium and the Fluid & DHI Consortium at the Colorado School of Mines and its participants for funding the project. We would also like to express our gratitude to Dr. Jeff Kenvin from Micromeritics for his insightful explanations about gas-adsorption theories, and to Dr. Arkadiusz Derkowski from Polish Academy of Sciences for all the discussion on clay microstructure. This paper has hugely benefited by the helpful suggestions and critical comments of Dr. Dave Dewhurst and an anonymous reviewer for Geophysical Prospecting.

REFERENCES

Ahmed S., Lovell C.W. and Diamond S. 1974. Pore sizes and strength of compacted clay: 14F, 2T, 15R. J. GEOTECH. ENGNG. DIV. V100, N.GT4, APR. 1974, P407-425. *International Journal of Rock Mechanics and Mining Sciences and Geomechanics Abstracts* **11**, A161.

Arne Johansen T., Ole Ruud B. and Jakobsen M. 2004. Effect of grain scale alignment on seismic anisotropy and reflectivity of shales. *Geophysical Prospecting* **52**, 133–149.

Aylmore L.A.G. and Quirk J.P. 1971. Domains and Quasi-Crystalline Regions in Clay Systems. *Soil Science Society of America Journal* **35**, 652–654.

Brown S.M. and Lard E.W. 1974. A comparison of nitrogen and mercury pore size distributions of silicas of varying pore volume. *Powder Technology* **9**, 187–190.

Brunauer S., Emmett P.H. and Teller E. 1938. Adsorption of gases in multimolecular layers. *Journal of the American Chemical Society* **60**, 309–319.

Bustin R.M., Bustin A.M., Cui X., Ross D., Murthy J.K., and Pathi V.S. 2008. Impact of Shale Properties on Pore Structure and Storage Characteristics. SPE 119892-MS. Presented at the SPE Shale Gas Production Conference, Fort Worth, Texas, USA, 16–18 November 2008.

Cases J.M., Berend I., Besson G., Francois M., Uriot J.P., Thomas F. and Poirier J.E. 1992. Mechanism of adsorption and desorption of water vapor by homoionic montmorillonite. 1. The sodium-exchanged form. *Langmuir* **8**, 2730–2739.

Clay Mineral Society Source Clay Information: http://www.clays.org/SOURCE%20CLAYS/SCdata.html.

Comisky J., Santiago M., McCollom B., Buddhala A. and Newsham K. 2011. Sample Size Effects on the Application of Mercury Injection Capillary Pressure for Determining the Storage Capacity of Tight Gas and Oil Shales. SPE-149432-MS, Presented at the Canadian Unconventional Resources Conference, 15–17 Nov, Alberta, Canada

Connell-Madore S. and Katsube T.J. 2006. *Pore-size Distribution Characteristics of Beaufort-Mackenzie Basin Shale Samples, Northwest Territories*. Natural Resources Canada, ISBN 0662436121.

Diamond S. 1970. Pore size distributions in clays. *Clays and Clay Minerals* **18**, 7–23.

Diamond S. 1971. A critical comparison of mercury porosimetry and capillary condensation pore size distributions of portland cement pastes. *Cement and Concrete Research* **1**, 531–545.

Drits V.A. and McCarty D.K. 2007. The nature of structure-bonded H2O in illite and leucophyllite from dehydration and dehydroxylation experiments. *Clays and Clay Minerals* **55**, 45–58.

Dubinin M.M. 1966. Porous Structure and Adsorption Properties of Active Carbons. In Philip L. Walker Jr. (Ed.), Chemistry and Physics of Carbon (Vol. 2, pp. 51–120). New York, U.S.A.: Marcel Dekker, Inc.

Dullien F.A.L. and Dhawan G.K. 1974. Characterization of pore structure by a combination of quantitative photomicrography and mercury porosimetry. *Journal of Colloid and Interface Science* **47**, 337–349.

Echeverria J.C., Morera M.T., Mazkiaran C. and Garrido J.J. 2008. Characterization of the porous structure of soils: Adsorption of nitrogen (77 K) and carbon dioxide (273 K), and mercury porosimetry. *European Journal of Soil Science* **50**, 497–503.

EIA's Energy in Brief: What is shale gas and why is it important? http://www.eia.gov/energy_in_brief/about_shale_gas.cfm.

Ewy R. and Morton E. 2009. Wellbore-Stability Performance of Water-Based Mud Additives. *SPE Drilling and Completion* **24**, 390–397.

Feoktistov N.A., Golubev V.G., Hutchison J.L., Kurduykov D.A., Pevtsov A.B., Ratnikov V.V. *et al*. 2001. TEM and HREM study of 3D silicon and platinum nanoscale assemblies in dielectric opal matrix. *Semiconductor Science and Technology* **16**, 955.

Gregg S.J. and Sing K.S.W. 1983. Adsorption, Surface Area, and Porosity (2nd ed.). New York: Academic press.

Groen J.C., Peffer L.A.A. and Pérez-Ramírez J. 2003. Pore size determination in modified micro-and mesoporous materials. Pitfalls and limitations in gas adsorption data analysis. *Microporous and Mesoporous Materials* **60**, 1–17.

Hornby E.B., Schwartz M.L. and Hudson A.J. 1994. Anisotropic effective-medium modeling of the elastic properties of shales. *Geophysics* **59**, 1570–1583.

ISO 9277:2010. 2010. Determination of the specific surface area of solids by gas adsorption – BET method.

Jaffe A. 2010. May 10, Shale gas will rock the world. The Wall Street Journal. Retrevied January 26, 2011, from http://online.wsj.com/article/SB10001424052702303491304575187880596301668.html.

Javadpour F. 2009. Nanopores and apparent permeability of gas flow in mudrocks (shales and siltstone). *Journal of Canadian Petroleum Technology* **48**, 16–21.

Joyner L.G., Barrett E.P. and Skold R. 1951. The determination of pore volume and area distributions in porous substances. II. Comparison between nitrogen isotherm and mercury porosimeter methods. *Journal of the American Chemical Society* **73**, 3155–3158.

Jullien M., Raynal J., Kohler É. and Bildstein O. 2005. Réactivité physicochimique des argiles: Outils pour l'évaluation de sûreté Physicochemical Reactivity in Clay-Rich Materials: Tools for Safety Assessment. *Oil and Gas Science and Technology – Rev. IFP* **60**, 107–120.

Katahara K.W. 1996. Clay mineral elastic properties. SEG Technical Program Expanded Abstracts: pp. 1691–1694.

Kim J.-W., Peacor D.R., Tessier D. and Elsass F. 1995. A technique for maintaining texture and permanent expansion of smectite interlayers for TEM observations. *Clays and Clay Minerals* **43**, 51–57.

Kuila U., Prasad M., Derkowski A. and McCarty D.K. 2012. Compositional Controls on Mudrock Pore-Size Distribution: An Example from Niobrara Formation. SPE 160141-PP. Presented at presentation at the SPE Annual Technical Conference and Exhibition held in San Antonio, Texas, USA, 8–10 October 2012.

Loucks R.G., Reed R.M., Ruppel S.C. and Jarvie D.M. 2009. Morphology, genesis, and distribution of nanometer-scale pores in siliceous mudstones of the Mississippian Barnett Shale. *Journal of Sedimentary Research* **79**, 848–861.

Lowell S., Shields J.E., Thomas M.A. and Thommes M. 2004. Micropore Analysis. *Characterization of Porous Solids and Powders: Surface Area, Pore Size and Density*, 101–128.

Luffel D.L. and Guidry F.K. 1992. New Core Anlaysis Methods for Measuring Reservoir Rock Properties of Devonian Shale. *Journal of Petroleum Technology* **44**, 1184–1190.

Mason G. 1982. The effect of pore space connectivity on the hysteresis of capillary condensation in adsorption-desorption isotherms. *Journal of Colloid and Interface Science* **88**, 36–46.

Militzer B., Wenk H.R., Stackhouse S. and Stixrude L. 2011. First-principles calculation of the elastic moduli of sheet silicates and their application to shale anisotropy. *American Mineralogist* **96**, 125–137.

Neaman A., Pelletier M. and Villieras F. 2003. The effects of exchanged cation, compression, heating and hydration on textural properties of bulk bentonite and its corresponding purified montmorillonite. *Applied Clay Science* **22**, 153–168.

Omotoso O., McCarty D.K., Hillier S. and Kleeberg R. 2006. Some successful approaches to quantitative mineral analysis as revealed by the 3rd Reynolds Cup contest. *Clays and Clay Minerals* **54**, 748–760.

Penumadu D. and Dean J. 2000. Compressibility effect in evaluating the pore-size distribution of kaolin clay using mercury intrusion porosimetry. *Canadian Geotechnical Journal* **37**, 393–405.

Pollastro R.M. 1992. Natural fractures, composition, cyclicity, and diagenesis of the Upper Cretaceous Niobrara Formation, Berthoud field, Colorado.

Prasad M., Kopycinska M., Rabe U. and Arnold W., 2002. Young's modulus of clay minerals using atomic force acoustic microscopy, *Geophysical Research Letters* **29**, 8.

Ross D.J.K. and Bustin R.M. 2009. The importance of shale composition and pore structure upon gas storage potential of shale gas reservoirs. *Marine and Petroleum Geology* **26**, 916–927.

Rouquerol J., Avnir D., Everett D.H., Fairbridge C., Haynes M., Pernicone N. *et al*. 1994. Guidelines for the characterization of porous solids. *Studies in Surface Science and Catalysis* **87**, 1–9.

Rouquerol J., Llewellyn P. and Rouquerol F. 2007. Is the BET equation applicable to microporous adsorbents? *Studies in Surface Science and Catalysis* **160**, 49–56.

Rouquerol J., Rouquerol F. and Sing K.S.W. 1998. *Absorption by Powders and Porous Solids*. Academic press, ISBN 0080526012.

Rutherford D.W., Chiou C.T. and Eberl D.D. 1997. Effects of exchanged cation on the microporosity of montmorillonite. *Clays and Clay Minerals* **45**, 534–543.

Sarker R. 2010. *Elastic and flow properties of shales*. PhD Dissertation, Colorado School of Mines.

Sayers C.M. 2005. Seismic anisotropy of shales. *Geophysical Prospecting* **53**, 667–676.

Sharp A.G. 1981. Design curves for oceanographic pressure-resistant housings. (WHOI Technical Memorandum 3-81). Woods Hole, Massachusetts: Woods Hole Oceanographic Institution. Retrieved from WHOAS: Woods Hole Open Access Server http://hdl.handle.net/1912/1427.

Sigal R.F. 2009. A methodology for blank and conformance corrections for high pressure mercury porosimetry. *Measurement Science and Technology* **20**, 045108.

Sills I.D., Aylmore L.A.G. and Quirk J.P. 1973. A comparison between mercury injection and nitrogen sorption as methods of determining pore size distributions. *Soil Science Society of America Journal* **37**, 535–537.

Sing K.S.W., Everett D.H., Haul R.A.W., Moscou L., Peirotti R.A. and Rouquerol J. 1985. IUPAC commission on colloid and surface chemistry including catalysis. *Pure and Applied Chemistry* **57**, 603–619.

Środoń J., Drits V.A., McCarty D.K., Hsieh J.C.C. and Eberl D.D. 2001. Quantitative X-ray diffraction analysis of clay-bearing rocks from random preparations. *Clays and Clay Minerals* **49**, 514–528.

Srodon J. and McCarty D.K. 2008. Surface area and layer charge of smectite from CEC and EGME/H2O-retention measurements. *Clays and Clay Minerals* **56**, 155–174.

Vanorio T., Prasad, M. and Nur, A., 2003. Elastic properties of dry clay mineral aggregates, suspensions and sandstones. *Geophysical Journal International* **155**, 319–326.

Webb P.A. and Orr C. 1997. *Analytical Methods in Fine Particle Technology*. Micromeritics Norcross, GA.